ADVANCED FUNCTIONAL MATERIALS
www.afm-journal.de

Ambient Manipulation of Perovskites by Alternating Electric Field toward Tunable Photovoltaic Performance

Zhendong Cheng, Dong Ding, Jingnan Song, Feng Liu, Tun Wang, Cheng Hu, Lixiang Ba, Jiayuang Wang, Hong Liu, and Wenzhong Shen**

With the rapid development of hybrid metal halide perovskites, controlling and understanding their growth processes have become an important but challenging task. In this paper, alternating electric field as an effective modulation method that acts on the intermediate state in perovskite formation under ambient conditions is introduced. The morphology and microstructure of the as-formed perovskites can be effectively controlled by tuning simple physical parameters such as the frequency and amplitude, which have shown strong impact on the motion of ionic species and thus influences the formation of materials. Furthermore, the optic and electronic properties of the perovskite (such as the band position) can also be easily tuned by the field parameters. Finally, a conversion efficiency of 19.08% can be achieved in $MAPbI_3$ device without any doping or additional treatment, with impressive ambient and thermal stability without encapsulation. This result has not only illustrated a new physical approach for material fabrication, but also facilitates deeper understanding of the formation mechanism and generally shed light to the development of more devices and materials.

1. Introduction

In recent years, hybrid metal halide perovskites have become more and more important for many advanced opto-electronic devices, profited by their advantages in optic absorption, carrier mobility, defect tolerance, and bandgap modulation with impressively low fabrication criteria.[1–5] The power conversion efficiency (PCE) of perovskite solar cells (PSCs) has surged from 3.8% by Miyasaka and co-workers[6] in 2009 to the unprecedented 25.2% in 2019,[7] on the way approaching theoretical limit of 31%.[8] However, severe challenges have yet remained with regard of their stability, scalability, building cost, and integration capability with other applicable devices (e.g., Si heterojunction solar cells[9]). To resolve that, tremendous efforts have been paid to the promotion of perovskites, such as interface engineering,[10] doping,[11] composition change,[12] additives,[13] and solvent engineering,[14] mostly chemical modifications mainly controlled by thermal diffusions and mechanical forces.

Nevertheless, significant obstacles are still standing in front of real applications. For the mainstream chemical approaching, more complexity, less reproducibility and higher costs could be brought by doping processes,[15–17] interfacial engineering,[18,19] alternation of contents, uncertainties during the fabrication (such as centrifugal force in spin-coating and motion of molecules in gaseous mediums in evaporation methods) and so forth. To resolve that, approaches by physical methods such as electromagnetic fields have been performed on the perovskite fabrication which have been reported to induce significant change in the structural and opto-electronic properties of materials.[20–22] Recently, some groups have found that some reversible morphological and structural responses (normally described as electrostrictive and electroelastic properties[23]) could be induced by certain external electric fields. Moreover, unlike classical perovskites and semiconductors, hybrid metal halide perovskites have shown excellent ion transport ability which has played an important part in their performance[24,25] and induced some unique behaviors in devices, e.g., significant hysteresis in *J–V* characteristics of PSCs.[26] Regarding those phenomena, they cannot be simply treated as classical ferroelectric or semiconducting materials in experimental and theoretical studies. What's more, it has been also found out that certain intermediate states (for example, $[PbI_6]^{4-}$) had existed as an important content in the sample during the formation of perovskite before the thermal annealing.[27] Therefore, more detailed studies on the consequence of external fields at different stages or under various ambient conditions would hopefully lead to better understanding of the perovskite formation and as well facilitate establishment of new methods for material manipulation. Especially, the alternating electric field with characteristic

Z. D. Cheng, D. Ding, T. Wang, C. Hu, L. X. Ba, J. Y. Wang, Dr. H. Liu, Prof. W. Z. Shen
Key Laboratory of Artificial Structures and Quantum Control (Ministry of Education)
Institute of Solar Energy
School of Physics and Astronomy
Shanghai Jiao Tong University
Shanghai 200240, P. R. China
E-mail: liuhong@sjtu.edu.cn; wzshen@sjtu.edu.cn
J. N. Song, Prof. F. Liu
Department of Polymer Science and Engineering
School of Chemistry and Chemical Engineering
Shanghai Jiao Tong University
Shanghai 200240, P. R. China
The ORCID identification number(s) for the author(s) of this article can be found under https://doi.org/10.1002/adfm.202004652.

DOI: 10.1002/adfm.202004652

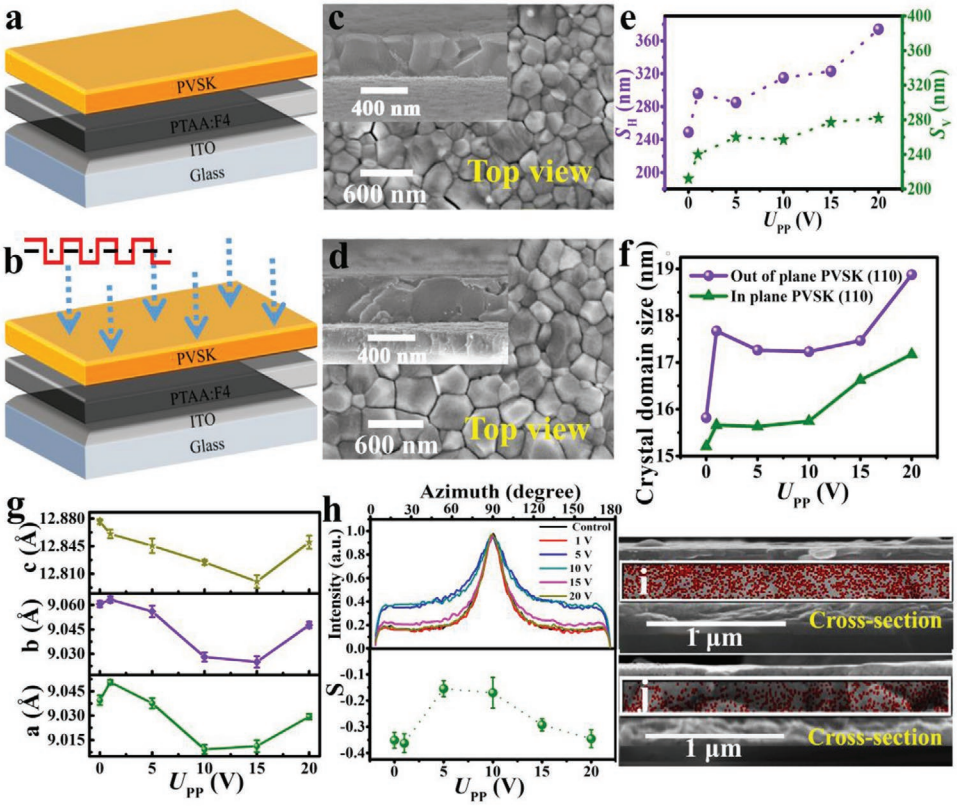

Figure 1. Illustration of the AEF method and morphological effect: a,b) Configuration of $MAPbI_3$ samples: a) without and b) with AEF, respectively; c,d) SEM top view of $MAPbI_3$ samples: c) without and d) with AEF (20 V, 20 Hz), respectively, insets showing corresponding cross-sectional view; e) Average horizontal grain size S_H and vertical size S_V versus the signal amplitude (U_{PP}), $f = 20$ Hz; f) in- and out-of-plane size of crystal domains versus field amplitude; g) lattice constants under different amplitudes; h) angular distribution of (110) domains (q_r near 0.99 $Å^{-1}$) and corresponding orientation order factor S; i,j) EDS cross-sectional scanning of $MAPbI_3$ samples: i) without and j) with AEF.

time scale close to the ion transport (10^{-1} to 10^{1} s) would be an interesting condition that could induce significant influence on the ionic systems in solid bulks.[28]

In this work, we will introduce a novel and facile modulation method of perovskites that applies alternating electric field (AEF) on the intermediate state during their formation processes, which can effectively induce significant morphological and structural reformation in tens of seconds in the atmosphere. The size of grains and crystal domains can be effectively influenced by variation of the field amplitude and frequency. Moreover, study of microstructures has indicated significant evolution of textures and lattice constant in the crystallites versus the filed parameters. These morphological and structural change have been evidently induced by the motion of some key ionic species under the influence of alternating electric field and thus lead to less defects, higher purity and controllable change of the band structure in the products. Consequently, the band positions can be well aligned to facilitate the injection of carriers to the adjacent charge transport layers and in the same time keep high intrinsic absorption with controlled bandgap. As a result, high performance p–i–n configuration $MAPbI_3$ PSCs could be realized with significantly higher efficiency (19.08%), J_{SC} (22.09 mA cm^{-2}) and V_{OC} (1.09 V) than the control sample without any doping or additional treatments. Moreover, the AEF perovskites have shown impressively higher ambient stability after long time exposure to the air without encapsulation and high thermal stability under high temperature compared to basic devices.[29] Further theoretical and experimental studies have shown that the enhancement of light absorption in the AEF samples has been aided by their higher roughness, while their stability enhancement could be at least partly due to their stronger hydrophobicity. On the whole, this work has indicated the importance of field-assisted motion of ionic species in the formation of perovskites and hopefully suggested a general way of facilitating novel fabrication methods for these materials via simple physical aspects.

2. Results and Discussion

2.1. Evolution of $MAPbI_3$ with AEF under Varied Field Amplitude

Firstly, the pristine samples have been fabricated by spin-coating method. The external electric field has been then applied on the spin-coated samples in air while thermal annealing was simultaneously conducted. The configuration of the setup is illustrated in **Figure 1**a,b (as well in Figure S1 in the Supporting Information). The thermal annealing of the control samples has also been carried out in air. The influence of the field intensity has been studied under varied applied voltage

with fixed electrode spacing and frequency (kept at 20 Hz, according to the characteristic time scale of ion transport in perovskite (≈10^{-1} to 10 s)).[28] As shown in Figure 1c,d, the AEF samples have shown significantly larger grain size than the control ones. The average horizontal size has been calculated using equivalent diameter of round shaped grain with the same area that has been statistically counted with large number of sampling, while the vertical size is estimated from the maximal height of a grain as it is similar to the film thickness (more details can be found in Figures S2 and S3 in the Supporting Information). The average horizontal and vertical sizes increase from about 295 and 240 nm at 1 V to 370 and 280 nm at 20 V, respectively (Figure 1e), showing a generally positive dependence on the field intensity. Meanwhile, the horizontal size is generally than the vertical size, and the rate of its increase is also faster versus the increase of voltage.

For a simplified explanation, this behavior could be possibly determined by two factors. First, increase of Gibbs free energy of nucleation ΔG_E could be additionally strengthened by the external electric field so that the growth process will be enhanced. The energy per unit volume given by the external electric field is proportional to the electrical conductivity and square of the field amplitude, so ΔG_E will be positively related to the increase of field intensity.[30–32] Therefore higher field intensity can accelerate the growth of existing nuclei. Second, the electric field could also increase the mobility of the reactive ionic species that can raise the reaction rate and enhance the formation of larger grains.[33] Consequently, larger grain size will lead to fewer grain boundaries, weaker recombination and better overall conductivity (Figure S4 in the Supporting Information), which is beneficial for higher device performance.[34] Nevertheless, too high voltage (>20 V) will lead to significant drop of absorption intensity at short wavelength that could be induced by larger pinholes under too high field amplitude (Figure S5 in the Supporting Information).

Moreover, as well-known, the grains of hybrid perovskites normally do not consist of uniform crystalline structures, but contain sub-grain crystallites called "crystal domains" with boundaries that cannot be displayed by SEM but detectable via other ways such as TEM (included in Figure S2 in the Supporting Information) and photoluminescence (PL).[35–37] The properties of crystal domains (size, microstructure) have played an important role in the opto-electric and ferroelectric properties of perovskites.[38–41] As shown in Figure 1f, the size of (110) crystal domains (main content in the $MAPbI_3$) has shown a generally positive dependence on the signal amplitude, with the in- and out-of-plane domain sizes increasing respectively from 15.1 and 15.8 nm for control sample to 17.1 and 18.8 nm for AEF sample at 20 V. These values have been calculated from the integrated intensity of (110) direction[42] in the grazing incidence X-ray diffraction (GIXRD) patterns (details can be referred from Figures S6 and S7 in the Supporting Information). The out-of-plane size is larger than the in-plane size but follows the similar trend of the latter. This is similar to the behavior of the grains and could have originated from similar mechanism.

Furthermore, the microstructural studies from GIXRD have shown a non-monotonic change of lattice constants versus the field intensity, with in general smaller a, b and c of the AEF samples than that of the control sample. The values of *a*, *b*, and *c* firstly change from 9.040, 9.058, and 12.878 Å (control sample) to 9.048, 9.065, and 12.865 Å (1 V), respectively. Then they decrease to 9.009, 9.023, and 12.803 Å (15 V) and then again increase to 9.028, 9.048, and 12.843 Å at 20 V, respectively (Figure 1g and Figure S8 in the Supporting Information). This phenomenon has indicated certain kind of field induced contraction in the perovskite lattices that has also be previously found in the electrochemical systems.[43] In the meantime, the microstructural studies also indicate that certain texture of the crystal domains has widely existed in the AEF sample. As for the (110) domains, measurements of the angular distribution of GIXRD have been taken and shown in Figure 1h, together with the calculated orientation order parameter *S* (*S* = –0.5, 0, 1 stand for edge-on, isotropic and face-on orientations, respectively. Details can be found in Figure S8 in the Supporting Information). It shows that as the voltage increased from 1 V, the orientation of (110) domains has changed from more like an edge-on situation to an almost isotropic arrangement at about 10 V, and then becomes edge-on again. Appearance of texture under AEF can be understood as the effect of electric force on the crystallites. However, the reason of the non-monotonic evolution versus field intensity change is still unknown. Probably a more detailed study on single crystals could be helpful for more information.

Apparently, certain ionic processes could have played important roles in those behaviors with so significant responses of material to the electric field in the low frequency range (similar characteristic time scale has been also reported in perovskite systems and claimed to be related to the motion of ionic species).[25,44] Hence the elemental distribution in the samples has also been investigated using energy-dispersive X-ray spectroscopy (EDS, Figure 1i,j, as well in Figure S9 in the Supporting Information). Compared to the control sample, the AEF perovskite has contained relatively more iodine content at the bottom of perovskite layer (near the substrate). Moreover, despite of different polarities, I^- and Pb^{2+} have an overall migration to the same direction under the electric field and finally accumulate at the same position (close to perovskite/HTL interface). This interesting phenomenon is consistent with some previous reports about the different transport mechanisms of ions in hybrid perovskite. According to that, the motion of Pb^{2+} is mainly in interstitial mode[45] and that of I^- is vacancy mediated, while the interstitial Pb^{2+} anions and I^- vacancies are both positively charged.[45–47] This will lead to migration of Pb^{2+} and I^- ions to the same direction in the perovskite bulk under electric field. What's more, the energy barriers in the sample[48,49] can induce a certain rectification effect that induces a one-directional motion of the ions/charged vacancies despite of the alternation of field direction. Generally, these factors will eventually lead to the overall redistribution of Pb^{2+} and I^- to the same direction under AEF conditions. These locally enriched ions could reduce the defect states in the perovskites and improve the optoelectronic performance of the materials (more detailed discussion can be found in Figure S10 in the Supporting Information).

2.2. Evolution of $MAPbI_3$ versus Frequency

Furthermore, when the frequency is varied, no significant change of the grain size can be observed (**Figure 2**, 0 Hz representing

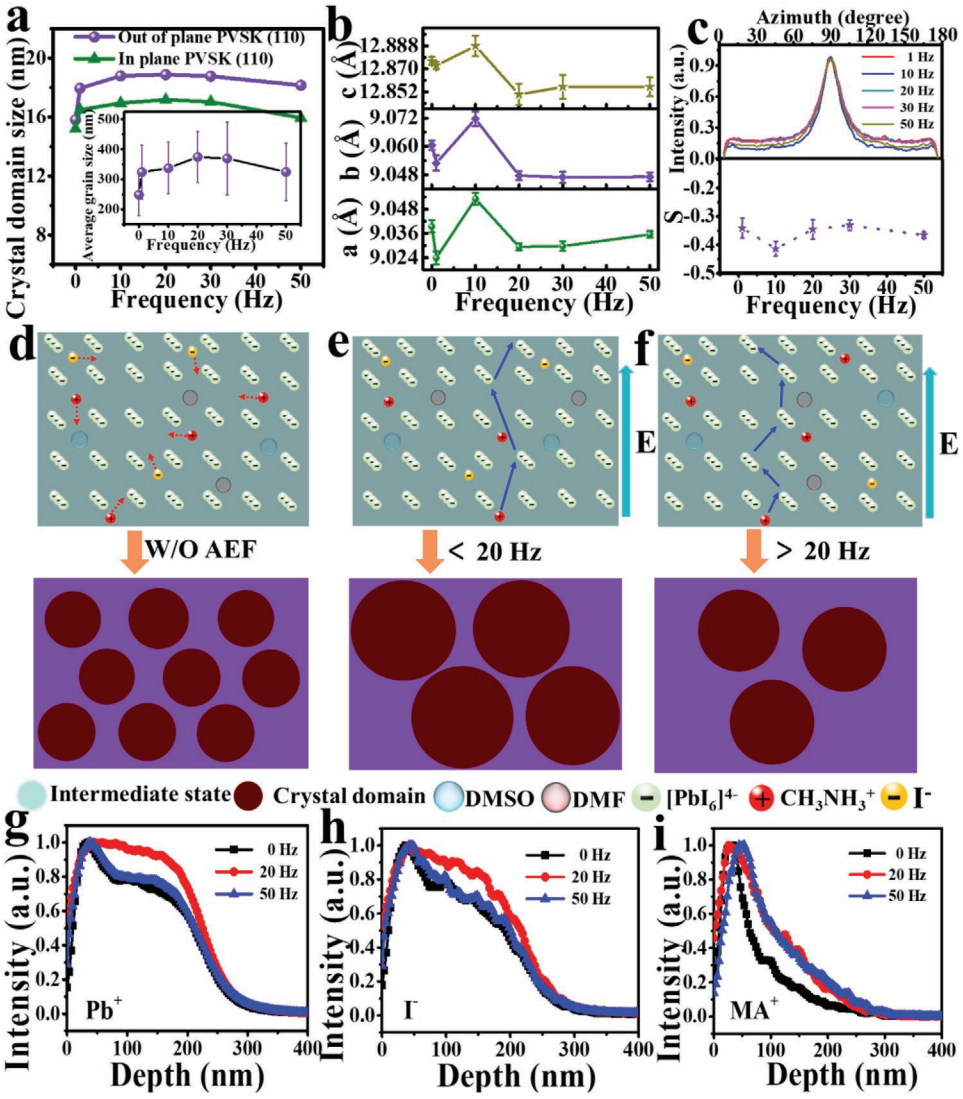

Figure 2. Perovskite under alternating electric field with frequency modulation: a) in- and out-of- plane size of crystal domain versus frequency, inset showing corresponding variation of the grain size; b) lattice constants versus the field frequency; c) angular distribution of (110) domains under different AEF frequency with corresponding orientation order parameter; d–f)Theoretical model of perovskite crystal domain expansion d) without AEF treatment; e) in low frequency region (<20 Hz) at 20 V and f) in high frequency region (30–50 Hz) at 20 V; g–i) SIMS results of different ionic species, all intensities are normalized: g) Pb^{2+}, h) I^{-}, i) MA^{+}.

the grain size of control sample), whereas the size of crystal domains exhibit non-monotonic variation versus the frequency (details can be found in Figures S11–S13 in the Supporting Information). For the control sample (indicated as the point at "0 Hz" in Figure 2a), the in- and out-of-plane (110) domain sizes are about 15.1 and 15.8 nm, respectively. Under AEF, the in- and out-of-plane domain size firstly increase with increasing frequency (<20 Hz), become largest (17.1 and 18.8 nm, respectively) at 20 Hz and then begin to decrease at frequency higher than 20 Hz. Moreover, with increasing frequency, the PbI_2 content firstly has a drastic increase and decrease near 1 Hz, reaches minimum at 20 Hz and then slowly increases again (Figure S13 in the Supporting Information). The PbI_2/perovskite ratio has shown the same trend. This indicates better purity of perovskite at 20 Hz, together with the largest grain and domain size.

To explain that, a possible model can be proposed as following. First, intermediate species exist in the as-formed sample mainly in the form of $[PbI_6]^{4-}$ after the deposition of precursors onto the substrate, according to preliminary research.[27] Their collision with MA^{+} ions will contribute to formation of the $MAPbI_3$ octahedral structure ruled by Goldschmidt tolerance factor $t = (r_A + r_I)/2^{1/2}(r_{Pb} + r_I)$,[50] and afterward the formation of perovskite domains. Since the mobility of $[PbI_6]^{4-}$ is much lower than the MA^{+} cations, the motion of MA^{+} will more likely play the main role in this process.[24,44] Second, the kinetic energy of the ions (Pb^{2+}, I^{-}, MA^{+}, $[PbI_6]^{4-}$) in the intermediate state is mainly from the thermal Brownian motion and the electric field. As being previously reported, the collisions require a minimum formation energy of 6 eV for $MAPbI_3$.[51] When no electric field is applied (Figure 2d), the movement of ions is

mainly in the form of Brownian motion (marked by red dashed arrows) from the volatilization of the solvent during the heating process. When an electric field is applied, more energy is transferred to the ions as the increment of their kinetic energy so that the formation of perovskite domains and grains will be further enhanced. The motion of ions in the intermediate state will be determined by the electric field and the damping force from the viscosity of the solution, which will accelerate and decelerate the ions, respectively. Because of the high damping effect in the intermediate mixtures, the field-induced increment of kinetic energy will be dissipated at the end of each accelerating period and therefore its maximum value is only determined by field induced acceleration in one single period.

At low frequency (Figure 2e), on the one hand, the increment of kinetic energy of ions will be higher in one longer acceleration period than that at high frequency. On the other hand, the number of collision events among MA^+ and $[PbI_6]^{4-}$ will increase with the frequency. Hence the formation of perovskite will be enhanced with increasing frequency under this condition. However, when frequency is too high (Figure 2f), the increment of kinetic energy of MA^+ cations will not be high enough to overcome the formation energy of 6 eV for perovskite by one much shorter acceleration period. Therefore, even if more collision events can take place under this condition, they would be futile for the formation of perovskite. The increment of kinetic energy will continue to decrease with shorter acceleration time (or in another word, higher frequency). Hence the total reaction probability decreases with the increasing frequency and so will be the domain size. As a result, the largest perovskite crystal domains are most easily formed in the moderate frequency range.

The results of microstructures have shown more complicate behavior than under the amplitude modulation (Figure 2b and Figure S14 in the Supporting Information). The values of *a*, *b*, and *c* first drop from 9.042, 9.059, and 12.873 Å (control sample) to 9.025, 9.050, and 12.870 Å (1 Hz), and then increase to 9.056, 9.069, and 12.895 Å at 10 Hz, respectively. Then those values decrease again to 9.030, 9.048, and 12.840 Å at 20 Hz and slowly increase with frequency to 9.033, 9.049, and 12.863 Å at 50 Hz, respectively. Except 10 Hz, most AEF conditions have appeared to result in smaller lattices than the case without electric field. The explanation for such complicate behaviors may require more precise control of crystallization and as well theoretical simulations. As for the texture (110) of crystal domains, no significant reorientation can be found versus the change of frequency, as shown in Figure 2c (other details can be found in Figure S14 in the Supporting Information). Different from the variation of domain size, it appears that the orientation of the crystal domains is dominantly influenced by the field amplitude, but almost insensitive to the frequency.

As shown above, significant structural change can be detected in the sub-grain level of the perovskite. To further study the change in the content, secondary ion mass spectroscopy (SIMS) has been carried out, as shown in Figure 2g–i. There's been significant redistribution of Pb^{2+}, MA^+ and I^- toward the perovskite/ITO interface in the AEF perovskites compared to the control sample (Specially, Pb^{2+} and I^- ions have more even distribution under 20 Hz than under other conditions). Such redistribution appears consistent with the EDX results shown in Figure 1f,g (as well in Figure S9, Supporting Information). What's more, the similar redistribution of MA^+ compared to Pb^{2+} has indicated that its motion is also mainly in interstitial mode like Pb^{2+}.[24,52] Noticeably, certain artifact of MA signal[53] can be observed in the region near the perovskite/ITO interface that could be induced by MA oxidation by O_2^+ sputtering, as has also been reported by some recent studies.[54] However, this will not influence the overall result that the general redistribution of MA^+ ions is toward perovskite/ITO interface since all measurements have been performed on samples with identical thickness and contents.

2.3. Optic and Electronic Properties of AEF $MAPbI_3$

As illustrated by previous sections, significant morphological and microstructural changes can be induced by AEF treated perovskites. Naturally, a question that follows would be their correlation with the opto-electronic properties of the materials. Steady PL and time-resolved photoluminescence (TRPL) have been carried out to survey the charge separation and collection in the interfaces and perovskite layer. Measurements have been first taken from top of perovskite with and without PCBM as the bottom layer to distinguish the influence of radiative recombination and charge transportation on the luminescence intensity.[55,56] In the case without PCBM, as shown in **Figure 3**a, the PL intensity of the AEF perovskite is at first (1 Hz) higher than the control sample, increases with increasing frequency until 20 Hz, and then decreases again to a value lower than the control sample. The high PL intensity at lower frequency (≤20 Hz) indicates weaker defect recombination and smaller trap density, as can be supported by the trap density space charge limited current measurements (Figures S15 and S16 in the Supporting Information). The decrease of PL at higher frequency (>20 Hz) could be due to more frequent MA^+ collisions under this condition, which have appeared not energetically effective to facilitate the formation of perovskite but enough to create more point defects according to previous discussion. Besides, the peak position has shown a slight red shift from 761 to 770 nm with increasing frequency (Figure 3a and Figure S17 in the Supporting Information), suggesting slight shrinking of bandgaps.

Furthermore, as being illustrated in Figure 3b, the AEF samples have shown much longer lifetime than that of the control sample (13.51 ns) at low frequency (≤20 Hz, reaching maximum of 36.77 ns at 20 Hz), which turns to be lower at frequency >20 Hz. This has indicated significant passivation effect of the defects inside perovskite layer. Like the PL, the decrease of lifetime at higher frequency (>20 Hz) could also be induced by enhanced collisions of the ionic species. All TRPL traces have been fitted using biexponential function as followed

$$I(t) = A_1 \exp\left(-\frac{t-t_0}{\tau_1}\right) + A_2 \exp\left(-\frac{t-t_0}{\tau_2}\right) + y_0 \quad (1)$$

where t_0 is the start time of decay process, y_0 is the background constant (neglectable in this work), and τ_1 and τ_2 are the fast and slow components derived from the fitting results, respectively. The first and second terms in Equation (1) correspond to the charge transfer and radiative decay, respectively.[57] The

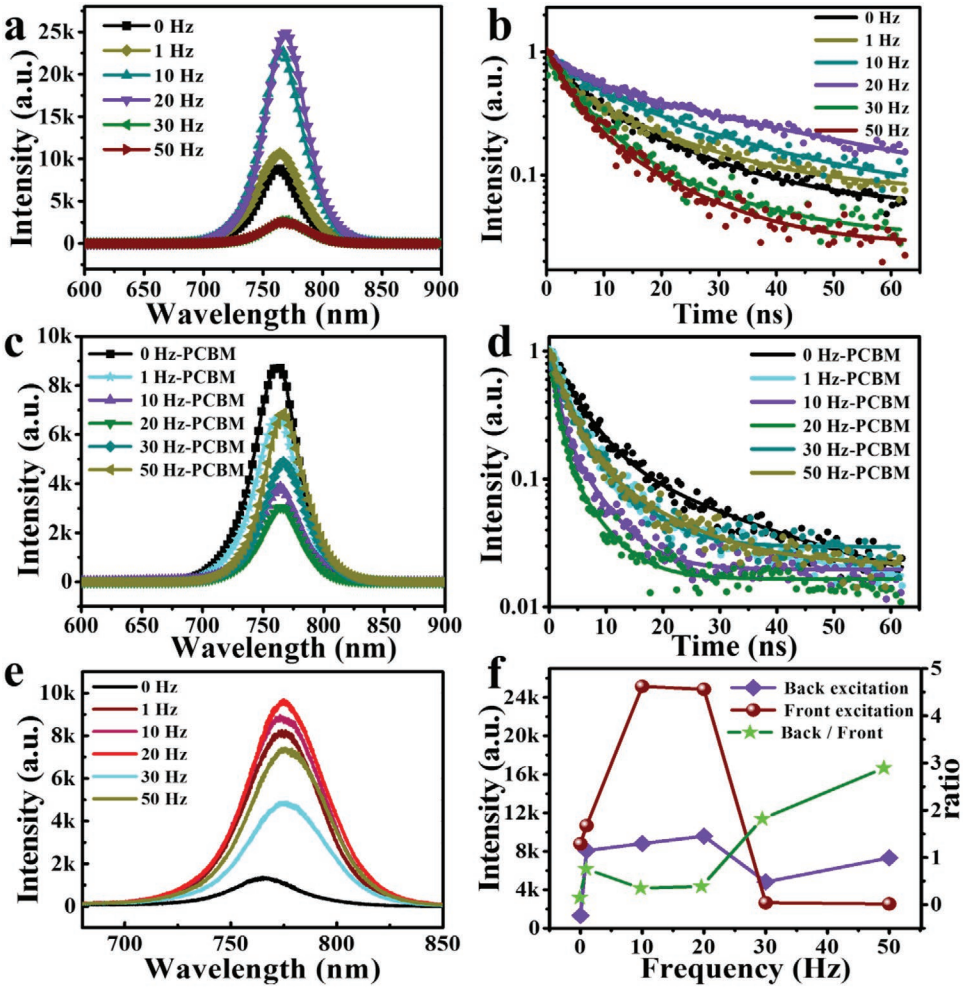

Figure 3. Photoluminescence property of perovskite under frequency modulation: a) PL and b) TRPL spectra of $MAPbI_3$ deposited on glass at 0, 1, 10, 20, 30, and 50 Hz (taken from the front excitation of $MAPbI_3$), dots and solid lines indicating original data and fitted curves, respectively; c) PL and d) TRPL spectra (intensity is normalized) of $MAPbI_3$ with PCBM at different frequencies; e) PL spectra of $MAPbI_3$ on glass, taken from the back excitation (the glass side); f) PL intensity versus frequency from the top and back side and their ratio, respectively.

mean carrier lifetime τ_{avg} can be obtained as following (details can be found in Table S1 in the Supporting Information)

$$\tau_{avg} = \frac{\sum A_n \tau_n^2}{\sum A_n \tau_n} \quad (2)$$

For case with PCBM, as shown in Figure 3c,d, the PL intensity of the AEF perovskites has been generally weaker than the control sample, while the TRPL has shown faster decay in the AEF samples. Such phenomena significantly indicate better carrier extraction and transport abilities of the AEF perovskites than the control sample. Especially, the shortest lifetime of ≈3.06 ns has been achieved at 20 Hz, which is much less than ≈14.12 ns of the control sample (details are listed in Table S2 in the Supporting Information). Therefore, the moderate frequency of 20 Hz has appeared to be the optimal condition for the improvement of electronic properties.

In addition, beside the measurements taken from the topside, PL has also been performed on backside (glass side) of the sample (Figure 3e). The PL spectra follow similar trend with the topside ones, indicating that the whole sample contains lowest defect density at 20 Hz. The ratio of the back/front excitation intensity of the AEF samples is generally larger than that of the control sample (point 0 Hz in Figure 3f). A possible reason is that certain accumulation of Pb and I species can take place at the bottom of perovskite bulk under AEF conditions (Figure 2 and Figure S9 in the Supporting Information), which can reduce the local bulk defect density and enhance the PL intensity with glass substrates.[58]

As commonly known, the electronic structure can also be influenced by changes in the morphology, microstructure, and composition of materials.[59] To verify that, the band structures of the samples have been investigated using UV–vis spectroscopy, as shown in **Figure 4**. In 500–650 nm, the absorbance first increases with the frequency, reaches maximum at 20 Hz and then decreases again (Figure 4a). In 650–850 nm, the absorption curves are quite close to each other. For the AEF sample at 20 Hz, its absorption is almost the same with the control sample at 500–650 nm but higher at 750–780 nm because of the shift of absorption edge. As being derived from the absorption

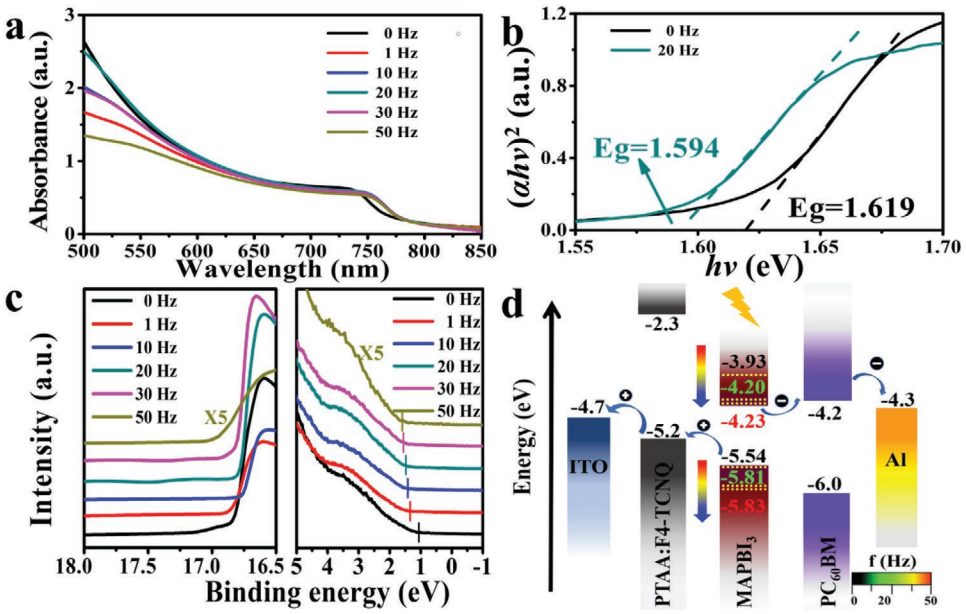

Figure 4. Electronic properties of $MAPbI_3$ under AEF with frequency modulation: a) Absorption spectra and b) Tauc plots of the fabricated $MAPbI_3$ films with different frequencies; c) UPS scans of cutoff edge spectra in the left panels and close-up of valence band onset shown the right hand side; d) energy band alignment for the $MAPbI_3$ device modulated by AEF at different frequencies (0, 20, and 50 Hz).

edge from Figure 4b, the bandgap of the optimized AEF perovskite film is about 1.594 eV, smaller than that of the control sample (1.619 eV), which could have been induced by more content of $MAPbI_3$ and less PbI_2 (with $E_g \approx 2.36$ eV)[60] in the AEF sample (Figure S13c, Supporting Information).

For more quantitative information, we have further analyzed the UPS spectra and calculated the band positions. As shown in Figure 4c, the change of bandgap appears to be quite slight versus different conditions (details are listed in Table S3 in the Supporting Information). In Figure 4d, the band positions under three representative conditions (without electric field, 20 Hz, 50 Hz) are displayed together with the typical energy diagram of a p–i–n structure cell, which indicate a general downward shift of the conduction and valence bands with increasing frequency. It can be noticed that the conduction band of AEF perovskite at 20 Hz is almost at the same level of the conduction band of the PCBM layer, while the valence band at 20 Hz is significantly lower than the hole transport layer but just slightly higher than the valence band at 50 Hz. First, lower position of the valence band of perovskite against the HTL will inhibit the reverse injection of holes from the HTL back to perovskite layer. Second, the conduction band of the perovskite layer should not be too low or its electron injection to the PCBM layer will drastically decrease even if it becomes just slightly lower than the conduction band of PCBM layer.[48,49] Finally, as discussed before, the change of the bandgap of perovskite is quite small under different conditions, so any shift of the valence band is accompanied with similar shift of the conduction band. Therefore 20 Hz has appeared to be the optimal frequency with balanced positions of the conduction and valence bands that lead to high performances[61] in corresponding solar cells. In general, the slight change of the absorption edge is possibly attributed to more $MAPbI_3$ content in the AEF samples compared the control ones.[60] The shift of the energy band could be originated from redistribution of ions in the perovskite bulk, as have been detected by previous elemental analysis by EDS and SIMS.[24,62] However, a more quantitative picture can be established aided by further theoretical investigation (e.g., calculation based on the first principle), while the correlation of the above optic-electronic properties with the morphological and structural evolution remains interesting topics to be explored.

2.4. Performance of AEF Perovskite in Photovoltaic Devices

Eventually, the as-fabricated materials have been integrated into typical p–i–n configuration PSCs (ITO/PTAA/$MAPbI_3$/$PC_{60}BM$/Al) to test their impact with common application, as shown in **Figure 5**. A comparison of the champion devices is illustrated in Figure 5a with *J–V* tests under standard AM 1.5 condition (detailed statistics can be found in Figures S18 and S19 in the Supporting Information). Compared to the control device (η = 16.53%, J_{SC} = 19.85 mA cm^{-2}, FF = 0.79, V_{OC} = 1.05 V), the AEF devices can achieve efficiency so long up to 19.08% (with J_{SC} = 22.09 mA cm^{-2}, FF = 0.79, V_{OC} = 1.09 V), which yields a 15.43% enhancement of efficiency. The J_{SC} values have matched well with the integrated EQE spectra shown in Figure 5b. Moreover, significantly higher and more stable output of PSCs with AEF perovskite has also been shown by the stabilized power output (SPO) measurement in Figure 5c compared to the control device. The higher V_{OC} and larger J_{SC} should be attributed to less carrier recombination and more effective charge transport at grain boundaries with larger grain size and less defects under alternating field. The statistical results are plotted in Figure 5d–f, with sample number of 50. These key parameters have shown much narrower distributions than the control samples, indicating quite satisfactory reproducibility and controllability of the AEF method.

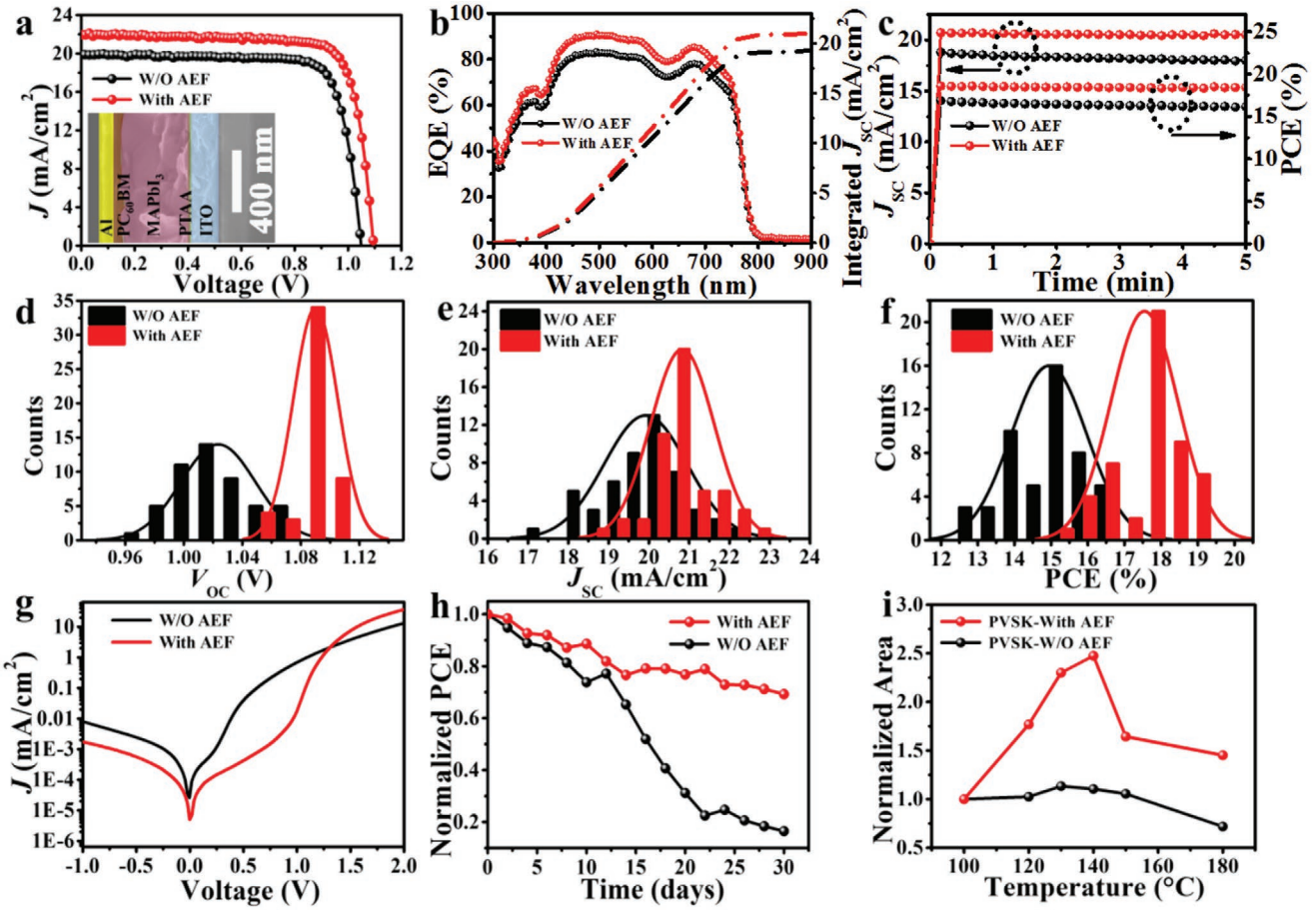

Figure 5. Characterization of device performance and stability test: a) *J–V* curves (reverse scanning) of the champion solar cells based on $MAPbI_3$ films fabricated without and with AEF (20 Hz, 20 V), the inset showing the cross-sectional SEM of corresponding PSC; b) Comparison of EQE and corresponding integrated J_{SC}; c) Comparison of steady-state power output (SPO); d–f) statistical histograms of d) V_{OC}; e) J_{SC} and f) efficiency of different devices; g) Dark *J–V* curves of the champion devices; h) Long-term stability of normalized PCE of unencapsulated $MAPbI_3$ devices stored in air (RH 70%, RT 25 °C); i) Content of perovskite under high temperature in the samples with and without AEF manipulation, with heating time 10 min.

Furthermore, the dark *J–V* measurement has also been applied to evaluate the charge recombination and transport processes.[63,64] As displayed in Figure 5g, the AEF PSC has shown lower dark current densities at negative bias than the control device. This difference suggests significant suppression of the leakage current in the AEF samples with fewer defects that could result in higher V_{OC} in the devices.[65,66] This is consistent with the observed PL results and the *J–V* characteristics shown in Figures 3 and 5d. At voltages from 1.3 to 2 V, the dark current of the AEF devices has a drastic increase, indicating more efficient electron injection capability.[67] For more quantitative description, the ideality factor *n* can be introduced as following

$$n = \frac{q}{kT}\frac{\partial V_{OC}}{\partial \ln J_{SC}} \tag{3}$$

where *q* is the elementary charge, *k* is the Boltzmann constant, and *T* is the absolute temperature. Smaller *n* indicates less carrier recombination.[67] Corresponding evaluated *n* values are 1.76 and 2.26 for the AEF and control sample, respectively (Figure S20 in the Supporting Information). Therefore, the former has shown apparently higher device quality.

Furthermore, as an intensively concerned property, the stability of the products has been verified via two different routes in this experiment. Firstly, the long term stability (with normalized PCE) of PSCs has been tested by the dark storage experiment (ISOS-D-1) based on recently proposed ISOS stability protocols (JV-3-5), which has been carried out in an air-filled (atmosphere with volume ratio of N_2/O_2 of 78:21) glovebox.[29] The PSC based on AEF treatment has maintained over 70% of the initial PCE after storage for 30 days at room temperature without encapsulation, whereas the one without AEF treatment has only retained below 20% of its initial efficiency. This result is comparable with the previous stability achievement on much more complicate systems.[68,69] The enhancement of stability could be induced by less defects/larger grains[34] and also the field induced contraction of lattices under AEF conditions, which could effectively inhibit the transport of external ionic species in the perovskite and therefore increase its intrinsic stability.[70]

Secondly, the thermal stability of the samples has been tested by heating process at temperature from 100 to 180 °C for 10 min in a nitrogen-filled chamber and then characterization by X-ray diffraction (XRD) measurements. The normalized (110) peak intensity has been used to identify the amount of perovskite in

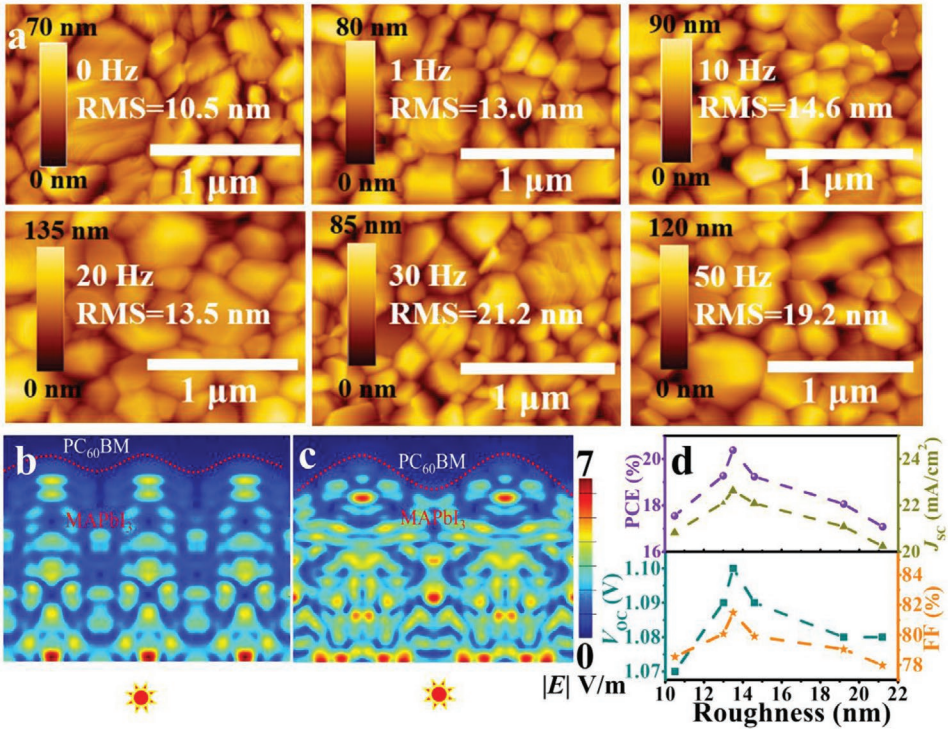

Figure 6. Surface condition and its influence: a) Typical AFM images of upper surface of AEF processed $MAPbI_3$, 20 V, f = 0–50 Hz; b,c) Calculated distributions of electric field in the samples: b) without and c) with AEF treatment on the interfaces of $MAPbI_3/PC_{60}BM$, with Wavy dashed lines represent the interface of $MAPbI_3/PC_{60}BM$; d) Simulation of photovoltaic parameters of PSCs as functions of film roughness.

the sample (details can be found in Figure S21 in the Supporting Information). As plotted in Figure 5i, the perovskite content in both samples will increase as the temperature increases from 100 to 130 °C, which could be regarded as facilitation on continuous crystallization process by low temperature annealing.[71,72] However, the amplitude of increase of the PEROVSKITE (110) composition in the AEF sample has been more significant than the control sample. This could be induced by more residual intermediate products in the AEF perovskites that can be converted into perovskite phase at elevated temperatures compared to the control samples (can be referred from GIXRD in Figure S10 in the Supporting Information).[27] At higher temperatures (140 °C for AEF treated one and 130 °C for control sample), the perovskite content begins to decrease versus the temperature, which could be most possibly related to the transition from $MAPbI_3$ to PbI_2. The higher turning point of the AEF sample has apparently shown its higher thermal stability, which could be induced by the larger grain size under alternating electric field. Overall, the AEF treated sample has shown significantly higher stability, which would be important for the application of PSCs under extreme conditions and could hopefully facilitate other systems (e.g., LEDs and sensors) as well.

2.5. Further Study on the Surface Situation and its Consequence

Beside the bulk properties, the surface situation of perovskite could have also played an important role in the device performance, as have been reported by many works. First, we have applied the atomic force microscopy (AFM) on the perovskite films to study their surface morphology. The root mean square (RMS) roughness of the $MAPbI_3$ interface increases from 10.5 to 21.2 nm as the frequency increases from 0 to 30 Hz (0 Hz indicates the control sample), and becomes slightly lower (19.2 nm) at 50 Hz (**Figure 6**a). Furthermore, we have carried out theoretical simulations utilizing Lumerical finite difference time domain (FDTD) software and Lumerical DEVICE software to calculate the field distributions in the bulk $MAPbI_3$ films and corresponding photovoltaic properties under illumination of the whole solar spectrum. Detailed parameters (carrier mobility, bandgap, defect density, refractive index) of each layer have been set according to previous literatures[73–78] (listed in Table S4 in the Supporting Information). Figure 6b,c presents the electric field distributions in the control device and the champion AEF device (with the roughness set at 10.5 and 13.5 nm, respectively) fabricated at 20 Hz under illumination, respectively. Apparently, the electric field intensity in the champion device is much stronger than the control sample. This could be due to enhanced Mie resonance scattering induced by larger perovskite grains in the AEF perovskites that can lead to more efficient coupling of the incident light with the photoactive layer and improvement of device performance.[79] Moreover, the detailed photovoltaic characteristics of simulated devices have been calculated and displayed as a function of roughness in Figure 6d. It can be seen too high roughness would result in lower performance, which could be attributed to the inhibition of charge extraction from PEROVSKITE to the hole transport layer by some previous report.[80] Theoretically,

the ultimate efficiency of the device (RMS ≈ 13.5 nm at 20 Hz) can be 20.5% higher than the experimental results so far in this work (Figure 5a). Therefore, further improvement of this AEF method on perovskites are yet expectable with the improvement of experimental details. Besides, the AEF films have also shown higher water contact angle than the control sample, indicating that they have more hydrophobic surfaces that could facilitate the long term stability of materials (Figure S22 in the Supporting Information).[81]

3. Conclusion

In this work, we have investigated a novel method using alternating electric field that can induce irreversible evolution of perovskites toward significant improvement of its optoelectronic properties. The morphology, microstructure and content in the perovskite can be effectively controlled by tuning the amplitude and frequency of the electric field. As a result, the band structure of the as-fabricated sample can be easily aligned by the field parameters. In the meantime, the alternating electric field processed samples have also shown higher purity and less defects. Finally, an impressive enhancement in the device performance could be achieved with $\eta \approx 19.08\%$ (15.4% higher than the control sample, with V_{OC} and J_{SC} respectively increasing from 1.05 to 1.09 V and 19.85 to 22.09 mA cm^{-2}) without additional materials and treatments. Furthermore, the as-fabricated samples have also shown significant enhancement in their long term stability under ambient and high temperature conditions without encapsulation. In addition, experimental and theoretical studies on the variation of surface conditions have also indicated the possibility to even higher performance ($\eta > 20\%$) in the future. In general, this work could not only facilitate the fabrication of perovskite materials and application of PSCs, but also give light to development of more methods and materials.

4. Experimental Section

Materials: Poly[bis (4-phenyl) (2,4,6-trimethylphenyl)amine] (PTAA, Mn = 3200, Mw = 4900), 2,3,5,6-tetrafluoro-7,7,8,8-tetracyanoquinodimethane (F4-TCNQ) and Lead iodide (PbI_2, 99.5%) were obtained from Xi'an Polymer Light Technology Corp. (China). Methylammonium iodide (MAI) was purchased from Deysol. [6,6]-phenyl C61-butyric acid methyl ester ($PC_{61}BM$, 99.5%) was purchased from Nano-C, Inc. (USA). All liquid reagents were purchased from Sigma-Aldrich, including *N*,*N*-dimethylformamide (DMF, anhydrous, 99.8%), Dimethylsulfoxide (DMSO, anhydrous, 99.8%), and Chlorobenzene (CB, anhydrous, 99.8%).

Material and Device Fabrication: The patterned ITO-coated glass substrates (1.7 cm × 1.7 cm, $R_s \leq 10\ \Omega\ \square^{-1}$, $T_r \geq 83\%$) were sequentially cleaned in an ultrasonic bath of diluted detergent, deionized water, acetone, and isopropanol (IPA) for 20 min in each step. After drying in a vacuum oven, they were treated with ultraviolet-ozone chamber (Jelight, USA) for 15 min and then transferred into an air-filled glovebox. For the hole transporting layer, 25% w/w F4-TCNQ doped PTAA was dissolved in CB to form a 1 mg mL^{-1} liquid precursor, which was then stirred and heated at 70 °C overnight. The mixture was spin-coated onto the ITO substrates at 5000 rpm for 30 s and subsequently annealed at 150 °C for 10 min in an air-filled glovebox (RH ≈ 20%). To improve the wettability of the PTAA film on the perovskite precursor, 60 µL DMF was spin-coated onto the PTAA/ITO substrates at 4000 rpm for 10 s. The perovskite precursor solution consists of PbI_2 (1.20 M), MAI (1 M, dissolved in mixed DMF/DMSO (9/1, v/v)), which was stirred at 60–70 °C overnight before the fabrication. Afterward, it was spin-coated onto the PTAA/ITO substrates at 4000 rpm for 30 s. 150 mL CB was quickly casted onto the product in the 5th second in the spin-coating process. Subsequently, the sample was transferred to a modulated electric field (device setup is shown in Figure S1 in the Supporting Information) with voltage from 0–20 V and electrode distance of 30 µm. The alternating electric field was generated by a function generator with power amplifier (Shenzhen ATTEN Technology Co. Ltd., ATF20F), with the parameters such as the waveform, amplitude and frequency set before operations. The AEF treated samples and control samples were all thermally annealed at 100 °C for 10 min. After cooling down to room temperature, 20 mg mL^{-1} $PC_{61}BM$ solution (in CB) was deposited on top of the perovskite layer at 1000 rpm for 60 s in the air-filled glovebox. All prepared solutions are filtered with poly(tetrafluoroethylene) filters (0.45 µm) before the spin coating. Finally, an Al (100 nm) electrode was thermally evaporated to the samples in vacuum (<6 × 10^{-4} Pa) through a shadow mask with active area of 0.05 cm^2.

Characterization: The surface morphology of the perovskite film and prepared PSCs has been observed by field-emission scanning electron microscope (FESEM, Zeiss Ultra Plus Germany) of the center for advanced electronic materials and devices (AEMD) and atomic force microscopy (AFM, Nanoscope IIIa Multimode). The elemental analysis has been performed by EDX installed in the SEM system (Oxford Instruments, Aztec X-Max 20). The GIXRD measurements were carried out in advanced light source (ALS), Lawrence Berkeley national laboratory (LBNL). The X-ray wavelength was 1.24 Å and the scattering intensity was measured by a PILATUS 2M detector and the measurement was performed in a closed chamber purged with helium to suppress air scattering. The integrated peak area, peak intensity and crystal size were obtained using IGOR software. High-resolution TEM (HRTEM) imaging (device model: FEI Talos F200X G2, operated at 200 kV) of $MAPbI_3$ are maintained at a low dose of ≈0.5 pA cm^2. The FIB treated specimens have been prepared using focused ion beam (FIB; Helios 600, FEI) equipped with C and Pt gas injectors and micromanipulator (Omniprobe). The 20 µm C layer has been deposited on the surface of the sample prior to the FIB cross-section preparation. The cross-sections measured about 8 × 13 µm^2 in area and 0.8 µm in thickness are cut off by 30 kV Ga^+ ions with ion beam current of 23 nA, removed from the bulk sample, and then attached to the Omniprobe semiring. Final thinning is performed with 30 kV Ga^+ ions (ion beam current 3 nA) followed by cleaning with 2 keV Ga^+ ions at beam current 10 pA. The time-of-flight secondary ion mass spectroscopy (SIMS, device model: TOF-SIMS 5, IONTOF, Germany) has been carried out with pulsed ion source from O^{2-} (1 keV) and Bi^+ (30 keV). The UV–vis absorption spectra were measured by UV–vis–NIR absorption spectrophotometer (LAMBDA750, Perkin Elmer, USA). The steady-state photoluminescence was measured by DAM302 (Horiba Jobin Yvon, FL, Japan) with excitation at 325 nm. The time-resolved photoluminescence spectra were collected with time-resolved fluorescence spectrofluorometer (Horiba Jobin Yvon, FL, Japan). A 400 nm pulsed laser with pulse width 1.3 ns was used to excite the samples from both front (perovskite film side) and back side (substrate side). Ultraviolet photoelectron spectroscopy (UPS) was carried out with an imaging photoelectron spectrometer (Thermo ESCALAB 250, USA) equipped with UV Light Source (He I = 21.2 eV) in an ultrahigh vacuum analysis chamber (<3 × 10^{-10} Torr), and the valence states of the prepared perovskite/ITO films were characterized by UPS He I measurements. The external quantum efficiency (EQE) spectra were acquired with Quantum Efficiency/IPCE system (PV Measurements Inc., QEX10) in the 300–900 nm wavelength range. No light soaking and bias voltage were applied during the measurement process. The photocurrent density–voltage (*J*–*V*) curves were measured by a Keithly 2400 sourcemeter under simulated AM 1.5G sunlight at 100 mW cm^{-2} irradiance by a 150 W class AAA solar simulator (XES-40S1, SAN-EI). Stabilized power output and stabilized photovoltage were also tested under standard 1 sun AM 1.5G in a N_2-filled glovebox. The long term stability test has been carried out under ambient conditions (in air at

1 atm, RH 70%, 25 °C) for 30 days. For the thermal stability measurement, each perovskite film was annealed in air at 100 °C for 10 min, and then aged at 100, 120, 130, 140, 150, and 180 °C in nitrogen atmosphere (1 atm, RH 10%, 25 °C) for 10 min, respectively.

Supporting Information

Supporting Information is available from the Wiley Online Library or from the author.

Acknowledgements

This work has been supported by the natural science foundation of China (11834011 and 11204176). The authors thank the center for advanced electronic materials and devices (AEMD) of Shanghai Jiao Tong University for the SEM measurement, and Prof. Zhiwen Shi of Shanghai Jiao Tong University for the KPFM measurement. We also thank the Instrumental Analysis Center of Shanghai Jiao Tong University for assistance of the TEM measurements. The authors are grateful to Ming Zhang at SJTU and Danqin Li at East China Normal University for the *J–V* test and EQE measurement. The authors also thank Prof. Feng Liu at LBNL for the GIXRD measurement and Jinqiu Xu at University of California, Berkeley for the probe of the sample morphology evolution. Finally, the authors acknowledge Peng Bai and Prof. Yueheng Zhang for helpful discussions over the manuscript and Runqian Wangyang for suggestions on the devices.

Conflict of Interest

The authors declare no conflict of interest.

Keywords

alternating electric field, grain formation, ion redistribution, perovskite, photovoltaics

Received: May 31, 2020
Revised: June 28, 2020
Published online:

[1] J. Burschka, N. Pellet, S. J. Moon, R. Humphry-Baker, P. Gao, M. K. Nazeeruddin, M. Gratzel, *Nature* **2013**, *499*, 316.
[2] M. A. Green, A. Ho-Baillie, H. J. Snaith, *Nat. Photonics* **2014**, *8*, 506.
[3] Q. Wang, Y. Shao, Q. Dong, Z. Xiao, Y. Yuan, J. Huang, *Energy Environ. Sci.* **2014**, *7*, 2359.
[4] C. Wehrenfennig, G. E. Eperon, M. B. Johnston, H. J. Snaith, L. M. Herz, *Adv. Mater.* **2014**, *26*, 1584.
[5] D. Shi, V. Adinolfi, R. Comin, M. Yuan, E. Alarousu, A. Buin, Y. Chen, S. Hoogland, A. Rothenberger, K. Katsiev, *Science* **2015**, *347*, 519.
[6] A. Kojima, K. Teshima, Y. Shirai, T. Miyasaka, *J. Am. Chem. Soc.* **2009**, *131*, 6050.
[7] National Renewable Energy Laboratory (NREL), NREL Best Research-cell Efficiency Chart, https://www.nrel.gov/pv/assets/pdfs/best-research-cell-efficiencies.20200218.pdf (accessed: January 2019).
[8] W. E. Sha, X. Ren, L. Chen, W. C. Choy, *Appl. Phys. Lett.* **2015**, *106*, 221104.
[9] K. Yoshikawa, H. Kawasaki, W. Yoshida, T. Irie, K. Konishi, K. Nakano, T. Uto, D. Adachi, M. Kanematsu, H. Uzu, K. Yamamoto, *Nat. Energy* **2017**, *2*, 17032.
[10] H. Zhou, Q. Chen, G. Li, S. Luo, T.-B. Song, H.-S. Duan, Z. Hong, J. You, Y. Liu, Y. Yang, *Science* **2014**, *345*, 542.
[11] B. Liu, S. Wang, Z. Ma, J. Ma, R. Ma, C. Wang, *Appl. Surf. Sci.* **2019**, *467*, 708.
[12] N. J. Jeon, J. H. Noh, W. S. Yang, Y. C. Kim, S. Ryu, J. Seo, S. I. Seok, *Nature* **2015**, *517*, 476.
[13] W. Ke, C. Xiao, C. Wang, B. Saparov, H. S. Duan, D. Zhao, Z. Xiao, P. Schulz, S. P. Harvey, W. Liao, W. Meng, Y. Yu, A. J. Cimaroli, C. S. Jiang, K. Zhu, M. Al-Jassim, G. Fang, D. B. Mitzi, Y. Yan, *Adv. Mater.* **2016**, *28*, 5214.
[14] N. J. Jeon, J. H. Noh, Y. C. Kim, W. S. Yang, S. Ryu, S. I. Seok, *Nat. Mater.* **2014**, *13*, 897.
[15] M. I. Saidaminov, J. Kim, A. Jain, R. Quintero-Bermudez, H. Tan, G. Long, F. Tan, A. Johnston, Y. Zhao, O. Voznyy, E. H. Sargent, *Nat. Energy* **2018**, *3*, 648.
[16] T. Bu, X. Liu, Y. Zhou, J. Yi, X. Huang, L. Luo, J. Xiao, Z. Ku, Y. Peng, F. Huang, Y.-B. Cheng, J. Zhong, *Energy Environ. Sci.* **2017**, *10*, 2509.
[17] A. L. Abdelhady, M. I. Saidaminov, B. Murali, V. Adinolfi, O. Voznyy, K. Katsiev, E. Alarousu, R. Comin, I. Dursun, L. Sinatra, E. H. Sargent, O. F. Mohammed, O. M. Bakr, *J. Phys. Chem. Lett.* **2016**, *7*, 295.
[18] A. Rajagopal, K. Yao, A. K. Jen, *Adv. Mater.* **2018**, *30*, 1800455.
[19] L. K. Ono, N.-G. Park, K. Zhu, W. Huang, Y. Qi, *ACS Energy Lett.* **2017**, *2*, 1749.
[20] Y. Lin, X. Ye, Z. Wu, C. Zhang, Y. Zhang, H. Su, J. Yin, J. Li, *J. Mater. Chem. A* **2018**, *6*, 3986.
[21] H. Röhm, T. Leonhard, A. D. Schulz, S. Wagner, M. J. Hoffmann, A. Colsmann, *Adv. Mater.* **2019**, *31*, 1806661.
[22] H. Wang, J. Lei, F. Gao, Z. Yang, D. Yang, J. Jiang, J. Li, X. Hu, X. Ren, B. Liu, J. Liu, H. Lei, Z. Liu, S. Liu, *ACS Appl. Mater. Interfaces* **2017**, *9*, 21756.
[23] B. Chen, T. Li, Q. Dong, E. Mosconi, J. Song, Z. Chen, Y. Deng, Y. Liu, S. Ducharme, A. Gruverman, F. Angelis, J. Huang, *Nat. Mater.* **2018**, *17*, 1020.
[24] Y. Yuan, J. Chae, Y. Shao, Q. Wang, Z. Xiao, A. Centrone, J. Huang, *Adv. Energy Mater.* **2015**, *5*, 1500615.
[25] C.-C. Zhang, Z.-K. Wang, M. Li, Z.-Y. Liu, J.-E. Yang, Y.-G. Yang, X.-Y. Gao, H. Ma, *J. Mater. Chem. A* **2018**, *6*, 1161.
[26] X. Cao, Y. Li, C. Li, F. Fang, Y. Yao, X. Cui, J. Wei, *J. Phys. Chem. C* **2016**, *120*, 22784.
[27] Q. Hu, L. Zhao, J. Wu, K. Gao, D. Luo, Y. Jiang, Z. Zhang, C. Zhu, E. Schaible, A. Hexemer, C. Wang, Y. Liu, W. Zhang, M. Gratzel, F. Liu, T. P. Russell, R. Zhu, Q. Gong, *Nat. Commun.* **2017**, *8*, 15688.
[28] H. Wang, A. Guerrero, A. Bou, A. M. Al-Mayouf, J. Bisquert, *Energy Environ. Sci.* **2019**, *12*, 2054.
[29] M. Khenkin, E. Katz, A. Abate, G. Bardizza, J. Berry, C. Brabec, F. Brunetti, V. Bulovic, Q. Burlingame, A. Di Carlo, R. Cheacharoen, C. Bing, A. Colsmann, S. Cros, K. Domanski, M. Dusza, C. Fell, S. Forrest, Y. Galagan, D. Girolamo, M. Grätzel, A. Hagfeldt, E. Hauff, H. Hoppe, J. Kettle, H. Köbler, M. Leite, S. Liu, Y. Loo, J. Luther, C. Ma, M. Madsen, M. Manceau, M. Matheron, M. McGehee, R. Meitzner, M. Nazeeruddin, A. Nogueira, Ç Odabaşı, A. Osherov, N. Park, M. Reese, F. Rossi, M. Saliba, U. Schubert, H. Snaith, S. Stranks, W. Tress, P. Troshin, V. Turkovic, S. Veenstra, I. Visoly-Fisher, A. Walsh, T. Watson, H. Xie, R. Yildirim, S. Zakeeruddin, K. Zhu, M. Lira-Cantu, *Nat. Energy* **2020**, *5*, 35.
[30] J. Tang, S. Li, X. Mao, Y. Du, *J. Phys. D: Appl. Phys.* **2005**, *38*, 729.
[31] Z. Hammadi, S. Veesler, *Prog. Biophys. Mol. Biol.* **2009**, *101*, 38.
[32] Ž. Janićijević, M. J. Lukić, L. Veselinović, *Mater. Des.* **2016**, *109*, 511.
[33] K. N. Ishihara, M. Maeda, P. H. Shingu, *Acta Metall.* **1985**, *33*, 2113.
[34] J. Feng, X. Zhu, Z. Yang, X. Zhang, J. Niu, Z. Wang, S. Zuo, S. Priya, S. F. Liu, D. Yang, *Adv. Mater.* **2018**, *30*, 1801418.
[35] S. Jariwala, H. Sun, G. W. P. Adhyaksa, A. Lof, L. A. Muscarella, B. Ehrler, E. C. Garnett, D. S. Ginger, *Joule* **2019**, *3*, 3048.
[36] Y. Zhou, H. Sternlicht, N. P. Padture, *Joule* **2019**, *3*, 641.

[37] W. Li, S. K. Yadavalli, D. Lizarazo-Ferro, M. Chen, Y. Zhou, N. P. Padture, R. Zia, *ACS Energy Lett.* **2018**, *3*, 2669.
[38] G. Zheng, C. Zhu, J. Ma, X. Zhang, G. Tang, R. Li, Y. Chen, L. Li, J. Hu, J. Hong, Q. Chen, X. Gao, H. Zhou, *Nat. Commun.* **2018**, *9*, 2793.
[39] Y. S. Teh, K. Bhattacharya, *J. Appl. Phys.* **2019**, *125*, 064103.
[40] Y. Zhou, A. L. Vasiliev, W. Wu, M. Yang, S. Pang, K. Zhu, N. P. Padture, *J. Phys. Chem. Lett.* **2015**, *6*, 2292.
[41] S. Xiao, H. Chen, F. Jiang, Y. Bai, Z. Zhu, T. Zhang, X. Zheng, G. Qian, C. Hu, Y. Zhou, Y. Qu, S. Yang, *Adv. Mater. Interfaces* **2016**, *3*, 1600484.
[42] J. Song, M. Zhang, M. Yuan, Y. Qian, Y. Sun, F. Liu, *Small Methods* **2018**, *2*, 1700229.
[43] F. Zhou, H. Liu, X. Wang, W. Shen, *Adv. Funct. Mater.* **2017**, *27*, 1606156.
[44] A. Walsh, S. D. Stranks, *ACS Energy Lett.* **2018**, *3*, 1983.
[45] C. Li, A. Guerrero, S. Huettner, J. Bisquert, *Nat. Commun.* **2018**, *9*, 5113.
[46] N. E. Courtier, J. M. Cave, J. M. Foster, A. B. Walker, G. Richardson, *Energy Environ. Sci.* **2019**, *12*, 396.
[47] J. M. Azpiroz, E. Mosconi, J. Bisquert, F. De Angelis, *Energy Environ. Sci.* **2015**, *8*, 2118.
[48] T. Minemoto, M. Murata, *Sol. Energy Mater. Sol. Cells* **2015**, *133*, 8.
[49] Y. Bai, X. Meng, S. Yang, *Adv. Energy Mater.* **2018**, *8*, 1701883.
[50] C. W. Myung, J. Yun, G. Lee, K. S. Kim, *Adv. Energy Mater.* **2018**, *8*, 1702898.
[51] P.-P. Sun, Q.-S. Li, L.-N. Yang, Z.-S. Li, *Nanoscale* **2016**, *8*, 1503.
[52] A. J. Knight, J. B. Patel, H. J. Snaith, M. B. Johnston, L. M. Herz, *Adv. Energy Mater.* **2020**, *10*, 1903488.
[53] S. P. Harvey, J. Messinger, K. Zhu, J. M. Luther, J. J. Berry, *Adv. Energy Mater.* **2020**, *8*, 1903674.
[54] C.-H. Hou, S.-H. Hung, L.-J. Jhang, K.-J. Chou, Y.-K. Hu, P.-T. Chou, W.-F. Su, F.-Y. Tsai, J. Shieh, J.-J. Shyue, *ACS Appl. Mater. Interfaces* **2020**, *12*, 22730.
[55] Q. Wang, E. Mosconi, C. Wolff, J. Li, D. Neher, F. De Angelis, G. P. Suranna, R. Grisorio, A. Abate, *Adv. Energy Mater.* **2019**, *9*, 1900990.
[56] Y. Liu, Q. Dong, Y. Fang, Y. Lin, Y. Deng, J. Huang, *Adv. Funct. Mater.* **2019**, *29*, 1807707.
[57] R. Cheng, C. C. Chung, H. Zhang, F. Liu, W. T. Wang, Z. Zhou, S. Wang, A. B. Djurišić, S. P. Feng, *Adv. Energy Mater.* **2019**, *9*, 1901980.
[58] T. Wu, M. Ahmadi, B. Hu, *J. Mater. Chem. C* **2018**, *6*, 8042.
[59] S. Premkumar, K. Kundu, S. Umapathy, *Nanoscale* **2019**, *11*, 10292.
[60] J. M. C. da Silva Filho, R. Landers, F. C. Marques, *J. Inorg. Organomet. Polym. Mater.* **2019**, *29*, 2161.
[61] J. Zhang, D. Bai, Z. Jin, H. Bian, K. Wang, J. Sun, Q. Wang, S. F. Liu, *Adv. Energy Mater.* **2018**, *8*, 1703246.
[62] C. Li, S. Tscheuschner, F. Paulus, P. E. Hopkinson, J. Kießling, A. Köhler, Y. Vaynzof, S. Huettner, *Adv. Mater.* **2016**, *28*, 2446.
[63] C. Chen, H. Li, J. Jin, X. Chen, Y. Cheng, Y. Zheng, D. Liu, L. Xu, H. Song, Q. Dai, *Adv. Energy Mater.* **2017**, *7*, 1700758.
[64] W. Ke, C. C. Stoumpos, I. Spanopoulos, M. Chen, M. R. Wasielewski, M. G. Kanatzidis, *ACS Energy Lett.* **2018**, *3*, 1470.
[65] C. Liu, K. Wang, C. Yi, X. Shi, A. W. Smith, X. Gong, A. J. Heeger, *Adv. Funct. Mater.* **2016**, *26*, 101.
[66] J. You, Y. Yang, Z. Hong, T.-B. Song, L. Meng, Y. Liu, C. Jiang, H. Zhou, W.-H. Chang, G. Li, Y. Yang, *Appl. Phys. Lett.* **2014**, *105*, 183902.
[67] X. Zhao, L. Tao, H. Li, W. Huang, P. Sun, J. Liu, S. Liu, Q. Sun, Z. Cui, L. Sun, Y. Shen, Y. Yang, M. Wang, *Nano Lett.* **2018**, *18*, 2442.
[68] J. A. Christians, P. Schulz, J. S. Tinkham, T. H. Schloemer, S. P. Harvey, B. J. Tremolet de Villers, A. Sellinger, J. J. Berry, J. M. Luther, *Nat. Energy* **2018**, *3*, 68.
[69] S. P. Dunfield, L. Bliss, F. Zhang, J. M. Luther, K. Zhu, M. F. A. M. van Hest, M. O. Reese, J. J. Berry, *Adv. Energy Mater.* **2020**, *13*, 1904054.
[70] H. Cho, S.-H. Jeong, M.-H. Park, Y.-H. Kim, C. Wolf, C.-L. Lee, J. H. Heo, A. Sadhanala, N. Myoung, S. Yoo, *Science* **2015**, *350*, 1222.
[71] Y. Hou, S. Yang, X. Chen, C. Li, H. Zhao, H. G. Yang, *Chem. - Eur. J.* **2017**, *23*, 5658.
[72] M. Saliba, K. W. Tan, H. Sai, D. T. Moore, T. Scott, W. Zhang, L. A. Estroff, U. Wiesner, H. J. Snaith, *J. Phys. Chem. C* **2014**, *118*, 17171.
[73] A. Yadav, S. Yadav, S. Singh, N. Tripathi, *Inter. J. Sci. Technol. Res.* **2002**, *1*, 108.
[74] W. Vervisch, S. Biondo, G. Rivière, D. Duché, L. Escoubas, P. Torchio, J.-J. Simon, J. Le Rouzo, *Appl. Phys. Lett.* **2011**, *98*, 253306.
[75] S. Zandi, M. Razaghi, *Sol. Energy* **2019**, *179*, 298.
[76] D. E. Motaung, G. F. Malgas, C. J. Arendse, S. E. Mavundla, *Mater. Chem. Phys.* **2012**, *135*, 401.
[77] S. A. Mauger, L. Chang, C. W. Rochester, A. J. Moulé, *Org. Electron.* **2012**, *13*, 2747.
[78] J. Diekmann, P. Caprioglio, M. Arvind, T. Unold, T. Kirchartz, D. Neher, M. Stolterfoht, D. Rothhardt, arXiv preprint arXiv:1910.07422, **2019**.
[79] T. Wang, D. Ding, H. Zheng, X. Wang, J. Wang, H. Liu, W. Shen, *Sol. RRL* **2019**, *3*, 1900045.
[80] H. Yu, J. Ryu, J. W. Lee, J. Roh, K. Lee, J. Yun, J. Lee, Y. K. Kim, D. Hwang, J. Kang, S. K. Kim, J. Jang, *ACS Appl. Mater. Interfaces* **2017**, *9*, 8113.
[81] J. C. Yu, S. Badgujar, E. D. Jung, V. K. Singh, D. W. Kim, J. Gierschner, E. Lee, Y. S. Kim, S. Cho, M. S. Kwon, M. H. Song, *Adv. Mater.* **2019**, *31*, 1805554.